

- 1
- 2
- 3
- 4
- 5
- 6
- 7
- 8
- 9
- 10
- 11
- 12
- 13
- 14
- 15
- 16
- 17
- 18
- 19
- 20
- 21

3
4
5
6
7
8
9
10
11
12
13
14
15
16
17
18
19
20
21

6
7
8
9
10
11
12
13
14
15
16
17
18
19
20
21

8
9
10
11
12
13
14
15
16
17
18
19
20
21

10
11
12
13
14
15
16
17
18
19
20
21

11
12
13
14
15
16
17
18
19
20
21

13
14
15
16
17
18
19
20
21

15
16
17
18
19
20
21

16
17
18
19
20
21

17
18
19
20
21

18
19
20
21

19
20
21

20
21

SUMMARY

As a size and shape selective catalyst, zeolites are widely used in petroleum and fine chemicals processing. However, their small micropores severely hinder molecular diffusion and are sensitive to coke formation. Hierarchically porous zeolite single crystals with fully interconnected, ordered and tunable multimodal porosity at macro-, meso- and micro-length scale like in leaves offer the ideal solution. However, their synthesis remains highly challenging. Here we report a versatile confined zeolite crystallization process to achieve these superior properties. Such zeolite single crystals lead to significantly improved mass transport properties by shortening the diffusion length while maintaining shape selective properties, endowing them with a high efficiency of zeolite crystals, enhanced catalytic activities and life time, highly reduced coke formation and reduced deactivation rate in bulky-molecule reactions and methanol-to-olefins process. Their industrial utilization can lead to the design of innovative and intensified reactors and processes with highly enhanced efficiency and minimum energy consumption.

KEYWORDS: hierarchical zeolites, zeolite single crystals, ordered structure, interconnected pores, improved diffusion rate, highly reduced coking, catalytic efficiency, catalytic cracking, MTO process

1 INTRODUCTION

2 Zeolites are one of the most important catalytic materials used today. Each zeolite
3 crystal can be considered as a catalytic reactor.¹⁻⁴ However, the slow transport of the
4 reactants and products within their intra-crystalline small microporous channels greatly
5 hinders their efficiency in catalysis and separation. It is highly desirable to reduce the
6 diffusion limitations within each zeolite crystal.⁵ The introduction of additional
7 interconnected intra-crystalline hierarchical mesopores or/and macropores is thus an
8 efficient strategy towards this.⁶⁻¹¹ In comparison with conventional demetalation
9 methods which are based on random removal of Al or Si atoms from zeolite frameworks
10 through acid or alkali leaching¹²⁻¹⁴ or chemical treatment,¹⁵ templating methods¹⁶⁻²⁸
11 allow precise control of the density and the size of additional mesopores or macropores,
12 generate much less defects in the zeolite framework and can avoid any negative impact
13 on crystallinity and active sites of the zeolite crystals. Tsapatsis et al. realized the
14 synthesis of size-tunable zeolite nanocrystals (MFI,¹⁷⁻¹⁹ BEA²⁰ and FAU²⁰) with various
15 intercrystalline mesoporosities using mesoporous carbon templates by steam-assisted
16 crystallization¹⁷⁻¹⁹ or hydrothermal synthesis²⁰ for improved catalytic performance in
17 ethanol dehydration.¹⁹ However, the synthesis of zeolite single crystals with
18 intracrystalline hierarchically porous structure still remain a great challenge. Schwiager
19 et al. very nicely synthesized microporous MFI-type (Silicalite-1,²¹ ZSM-5,^{22,23} TS-1²⁴)
20 zeolite single crystals by steam-assisted crystallization of mesoporous silica spheres.
21 The embedded intracrystalline macropores in ZSM-5 zeolite and TS-1 zeolite can
22 significantly improve the catalyst performance in the methanol to olefins (MTO)
23 reaction^{22,23} and the liquid phase epoxidation of 2-octene.²⁴

24 The interconnectivity between the intrinsic microporosity of zeolites and
25 additional meso- or/and macroporosity is essential to improve their mass transport
26 properties.⁵ This leads to a better accessibility to the active sites located within the
27 micropore system of the zeolites.²⁹ Many advanced techniques are developed to probe
28 the interconnectivity of the pores.³⁰ Pérez-Ramírez et al. contributed greatly to get
29 insight into the interconnectivity of the hierarchical pores,³¹ including the gas
30 adsorption studies,³² mercury porosimetry,³³ gravimetric uptake of bulking alkanes,³⁴
31 infrared spectroscopy of substituted alkylpyridines with different size³⁵ and positron
32 annihilation lifetime spectroscopy.^{36,37} In the same way, advanced imaging techniques
33 based on electron tomography and rotation electron diffraction,^{21,28} continuous-flow
34 variable-temperature hyperpolarized ¹²⁹Xe nuclear magnetic resonance(NMR)^{38,39} and
35 pulsed field gradient (PFG) NMR^{40,41} have also proven to be powerful tools for
36 assessing the pore interconnectivity in hierarchically structured zeolites.

37 More precise control over the location and interconnectivity of the additional
38 porosity could offer potential gains from the structural modification.⁴² To address this,
39 a cationic amphiphilic copolymer was designed by Liu et al.²⁷ to synthesize ZSM-5
40 zeolite single crystalline sheets with abundant and highly interconnected b-axis-aligned
41 mesoporous channels. This approach resulted in much higher catalytic activities for
42 bulky molecules conversion than bulk ZSM-5 and ZSM-5 with randomly oriented
43 mesopores while the stability and shape selectivity need further improved.²⁷ Many

1 classes of organisms both in plants and animals contain hierarchical networks of
2 interconnected pores to maximize mass transport and rates of reactions for the highest
3 efficiency and the lowest energy consumption. It is thus highly desirable to construct
4 such hierarchical networks of interconnected pores within each of zeolite crystals.
5 However, hierarchically structuring tunable mesoporosity and macroporosity
6 simultaneously with excellent interconnectivity, desired location and high ordering
7 within each zeolite single crystal to maximize the benefits of the porous hierarchy in
8 catalytic reactions still remains highly challenging.^{10,42}

9 We report synthesis of ZSM-5 zeolite single crystals with a fully interconnected
10 and highly ordered intra-crystalline macro-meso-microporous hierarchy in all
11 directions like in leaves through a versatile templating strategy via an in-situ bottom-
12 up confined zeolite crystallization process (Figure 1). The unique hierarchical structure
13 of our single zeolite crystals with high thermal and hydrothermal stability and excellent
14 mechanic strength can maximize the intracrystalline diffusion rate of reactants and
15 products and the accessibility to active sites, for example, the effective diffusion rate of
16 molecules in our zeolite single crystals reaches 10 and 5 folds higher than that of
17 benchmark commercial micro-sized mesoporous ZSM-5 and the state-of-the-art
18 nanosized macroporous ZSM-5, respectively. The efficiency of each of our zeolite
19 single crystals in bulky 1,3,5-triisopropylbenzene (TIPB) cracking reaction can reach a
20 high value of 0.84, which is doubled compared to that of benchmark commercial ZSM-
21 5 catalyst and 20% higher than that of the state-of-the-art nanosized ZSM-5 catalyst.
22 All these excellent properties lead to a significant reduction in coking and deactivation
23 rate, outstanding catalytic activity and selectivity and highly improved catalyst lifetime
24 in bulky molecules reactions and methanol-to-olefins (MTO) process. The average
25 coking rate in MTO reaction using our zeolite single crystals can reach 8.9 and 7.2 times
26 lower and their life time can be extended 13 and 3.5 times longer than that for
27 benchmark commercial micro-sized mesoporous ZSM-5 and the state-of-the-art
28 nanosized macroporous ZSM-5, respectively. It is envisioned that the catalytic reactor
29 can be made solely by zeolite single crystal. The excellent performance of zeolite single
30 crystals can be fully exploited in the catalytic reactions without any negative effect of
31 binder and additives with much highly enhanced efficiency, high catalytic activity,
32 selectivity and life time, minimum energy, time and raw material consumption. Most
33 importantly, the up-scalable and versatile synthesis strategy has been used to synthesize
34 single crystals of any kind of zeolite structures and zeotype materials and can be
35 extended to fabricate single crystalline solids of any chemical compositions such as
36 transition metal oxides (TiO₂, ZnO, ...), phosphate compounds, silicate compounds,
37 perovskites,... These new hierarchically meso-macroporous materials with single
38 crystalline nature will open a large panel of applications not only in adsorption, catalysis
39 and separation, but also in energy storage and conversion and create new research areas.

RESULTS AND DISCUSSION

Hierarchical Zeolite Single Crystals.

Hierarchically ordered macro-mesoporous carbon (OMMC, Figures 1B and S1) with an inverse opal structure is used as the meso-macroporous template.^{43,44} The key advantage is that such a template provides a confined and tailorable space for the formation of well-shaped hierarchically porous zeolite single crystals (Figures 1C and 1D). The synthesis of such uniform zeolite single crystals involves three steps: 1) infiltration of zeolite precursor slurry into OMMC template (Step 1 in Figure 1), 2) steam-assisted crystallization (SAC) of precursors confined in OMMC template (Step 2 in Figure 1), and 3) template removal (Step 3 in Figure 1). Each zeolite single crystal is made up of an assembly of tightly interconnected small zeolite spheres in a close-packed FCC arrangement (Figure 1E), which inherits the highly ordered FCC structure of the original polystyrene opalline crystal structure for the OMMC template fabrication (Figure S2). The FCC arrangement of these tightly interconnected small zeolite spheres results in the formation of tetrahedral (T_d) and octahedral (O_h) voids by 4 and 6 spheres from two layers (Figures 1F and S3-S5, Video S1), respectively. Such periodically arranged T_d and O_h voids within one zeolite single crystal, in addition to the intrinsic microporosity of zeolite, provide ordered, fully interconnected meso- and macroporous structure (Figure 1G and Video S1), precisely replicating the OMMC template (Figure S1).

As proof of concept, hierarchically ordered and highly interconnected macro-meso-microporous ZSM-5 single crystals with a tunable Si/Al molar ratio from 30 to ∞ and tunable mesopore and macropore size have been synthesized. We denote the as-synthesized samples as OMMS-ZSM-5(x,y); OMMS represents ordered macro-mesoporous zeolite single crystals, whereas x and y indicate the macropore size (nm) of the OMMC templates and the obtained Si/Al molar ratio, respectively.

Scanning electron microscope (SEM) images show that after 10 h crystallization, all the crystals of OMMS-ZSM-5(400,30) used as a representative sample for illustration exhibit a truncated hexagonal prism morphology (Figures 2A-2D). Although the size of the OMMC template is tens of microns, the obtained zeolite single crystals are well shaped with a similar crystal size of 4-5 μm (Figure 2A). The final size and the uniformity of the zeolite single crystals are highly dependent on the mass ratio of SiO_2 and OMMC template ($m\text{SiO}_2/m\text{OMMC}$) and the crystallization time (Figures S6-S7). When $m\text{SiO}_2/m\text{OMMC}$ mass ratio is low, the macropores of the OMMC template can only partly be filled by the dry gel, only several zeolite single crystals with different crystal size are obtained (Figure S6) while at high $m\text{SiO}_2/m\text{OMMC}$ ratio, all the porosities of the OMMC template can be fully filled by the dry gel, the uniform zeolite single crystals are formed. With increasing the crystallization time to 10h, zeolite single crystals reach their maximum size of 4-5 μm (Figure S7). The highly ordered arrangement of uniformly sized and tightly interconnected small zeolite spheres can be clearly visualized from three different directions in the representative SEM images (Figures 2B-2D) and the corresponding schematic illustrations (Figures 2E-2G) of one individual zeolite crystal. Typical high-angle annular dark field scanning

transmission electron microscope (HAADF-STEM) images reveal that tightly packed and inter-grown spheres are imprinted in a highly ordered arrangement within one entire zeolite crystal of OMMS-ZSM-5(400,30), indicating a positive replication of the OMMC template. The diameter of the small zeolite spheres is ~ 400 nm (Figure 2H), identical to the macropore size of the OMMC template and slightly smaller than the size of the PS spheres (~ 420 nm) used for the OMMC template fabrication (Figure S2). The corresponding selected area electron diffraction (SAED) pattern of one zeolite crystal (Figure 2H inset) contains discrete diffraction spots and can be indexed according to the MFI type zeolite along the [010] zone axis, providing the clear evidence of the single-crystalline nature of OMMS-ZSM-5(400,30). By indexing the diffraction pattern, the crystal facets can be readily identified. The largest facets, oriented perpendicular to the electron beam, are (010)-type, while the smaller side facets are (101) and (001)-type. The dominance of the (010) surface facets can be explained by the MFI-type zeolite crystal preferential growth direction, being in accordance with theoretical calculations predicting the lowest surface energy for the (010) facet.²⁷ A typical joint between two spheres can be seen in Figure 2I. SAED patterns taken from three different regions of the joint (Figure 2I zone 1 to zone 3) show that the two spheres, including the half sphere on the left (Figure 2J), the joint area (Figure 2K) and the sphere on the right (Figure 2L), all have the same [001] orientation. This unequivocally confirms the continuous crystalline phase in the same axis. The high resolution transmission electron microscopy (HRTEM) image (Figure 2M and inset) of the area indicated by the green rectangle in Figure 2I further reveals a continuous, uniform and dislocation free lattice arrangement at the joint over the entire image region. No (sub)grain boundaries or interfaces are observed. This proves that all the spheres organized in an FCC arrangement are not independent but crystallized in the same orientation and intergrown to form the entire zeolite single crystal. Besides, no planar defects such as stacking faults, twin formation or dislocations are observed, confirming the pristine structure throughout the zeolite crystal.

X-ray diffraction (XRD) pattern of OMMS-ZSM-5(400,30) is compared with standard PDF card (Figure 2N), confirming the formation of a pure MFI zeolite phase with excellent crystallinity. The intrinsic microporosity of zeolite single crystals is determined using Ar adsorption while N₂ adsorption is adopted to investigate the mesoporosity. OMMS-ZSM-5(400,30) shows type I isotherms with a micropore size distribution centered at 5.3 Å, characteristic of ZSM-5 zeolite with 10-membered ring channels (Figure 2O and inset).⁴⁵ The micropore surface area and volume of OMMS-ZSM-5(400,30) are 299 (m²g⁻¹) and 0.14 (cm³g⁻¹), respectively (Table S1), indicating that the formation of a hierarchically macro-mesoporous system does not influence its inherent microporous structure. The existence of mesopores in OMMS-ZSM-5(400,30) is confirmed by N₂ adsorption-desorption experiments. The steep adsorption of N₂ in the $0.6 < p/p_0 < 1.0$ region corresponds to the capillary condensation in the mesopores (Figure S8A), with the mesopore size distribution centered at 35 nm. The mesoporous surface area and total volume are 166 (m²g⁻¹) and 0.27 (m³g⁻¹) (Table S1), respectively. The presence of meso- and macropores in OMMS-ZSM-5(400,30) is fully confirmed by means of mercury intrusion porosimetry measurement showing (inset of Figure 2P)

1 a narrow mesopores distribution centered at ~35 nm, same as the value obtained by the
2 N₂ adsorption, and a broader macroporous distribution centered at ~100 nm. These
3 interconnected and periodically ordered mesopores and macropores stem from the
4 tetrahedral and octahedral voids within OMMS-ZSM-5 single crystals, respectively
5 (Figure 1G). The presence of the highly ordered mesopores of 35 nm and macropores
6 of 100 nm is also evidenced by the theoretical calculation and TEM and SEM
7 observations (Figures S4 and S5), showing the consistence between the results obtained
8 from N₂ adsorption, mercury intrusion, theoretical calculations and TEM and SEM
9 observations. The ²⁷Al MAS NMR spectrum (Figure S9A) indicates that aluminum
10 atoms solely exist in the tetrahedral position ($\delta = 55$ ppm) and no extra-framework
11 aluminum species ($\delta = 0$ ppm) are found. The ²⁹Si MAS NMR spectrum (Figure S9D)
12 shows that the framework primarily consists of crosslinked Q⁴ silica units [$\delta = -114$
13 ppm, Si(OSi)₄] and Q³ silica units [$\delta = -106$ ppm, Si(OSi)₃(OH) and/or Si(OSi)₃(OAl)]
14 without Q² units, indicative of complete condensation of the framework.

15 HAADF-STEM (Figure 3A) and 3D electron tomographic reconstruction (Figure
16 3B and Video S2) of OMMS-ZSM-5(400,30) demonstrate again that each zeolite single
17 crystal is constructed by densely stacked and tightly interconnected small zeolite
18 spheres of ~400 nm diameter. For a better visualization of the arrangement of the
19 intergrown small zeolite spheres, slices along three different axes are shown in Video
20 S2. For the slices along the Y-axis, two neighboring layers in OMMS-ZSM-5(400,30)
21 (Figures 3E-3F) correspond to the (010) planes in an FCC arrangement (Fig. 3c).
22 Similarly, for the slices along the Z-axis, two neighboring layers in OMMS-ZSM-
23 5(400,30) (Figures 3G-3H) correspond to the (-101) planes in an FCC arrangement
24 (Figure 3D). These results confirm that small zeolite spheres are densely stacked in a
25 close-packed FCC arrangement within an individual zeolite single crystal, consistent
26 with the inverse opal structure of the carbon template (Figure S1). It is important to
27 note that these small uniform zeolite spheres are all tightly interconnected by the joints
28 (Figures 3C-3H and Video S2), which are formed due to the simultaneous formation of
29 small zeolite spheres through the windows connecting macropores of the OMMC
30 template (Figure S1). All the above results clearly demonstrate that highly crystalline
31 zeolite single crystals with a hierarchically porous network with fully interconnected,
32 ordered and multimodal porosity at macro-, meso- and micro-length scale like in leaves
33 are obtained.

34 The diameter of the spheres in OMMS-ZSM-5 single crystals can be tuned from
35 200 to 600 nm by using OMMCs with different macropore sizes (Figure S1), resulting
36 in tunable tetrahedral and octahedral voids and thus, tunable intra-crystalline mesopore
37 and macropore sizes in each zeolite single crystal (Figures S10-S12 and Table S1). The
38 Si/Al ratio of OMMS-ZSM-5 can also easily be tuned from 30 to ∞ (Figures S13-S15).
39 The excellent mechanical, thermal and hydrothermal stability (Figure S16) of our
40 OMMS-ZSM-5 single crystals have been evidenced through a series of high pressure
41 and high temperature treatment with/without vapor. The poor (hydro)thermal stability
42 of the Nano-ZSM-5 (Figure S17) compared to those of zeolite single crystals with
43 ordered intra-crystalline macro-meso-microporous hierarchy further demonstrates the
44 superiority of zeolite single crystals. Such high stability of zeolites under very severe

conditions is of great importance for their catalytic applications.

Catalytic Performance in Bulky Molecules Cracking and MTO.

The significant superiority of such unique hierarchical porous structure of our zeolite single crystals is first revealed in the catalytic cracking of bulky 1,3,5-triisopropylbenzene (1,3,5-TIPB) (Table S2). The benchmark commercial micro-sized mesoporous ZSM-5 (C-ZSM-5) and the state-of-the-art nanosized macroporous ZSM-5 (Nano-ZSM-5) have been used as reference catalysts. The detailed adsorption-desorption and SEM characterization (Figures S18-S19 and Table S1) shows clearly that the benchmark C-ZSM-5 has mesopores at 2 nm and the state-of-the-art Nano-ZSM-5 has macropores at 51 nm. These two samples containing hierarchically multiple porosity (micro-mesopores for the benchmark C-ZSM-5 and micro-macropores for the state-of-the-art Nano-ZSM-5) are thus excellent references for comparison with our micro-meso-macroporous zeolite single crystals. The benchmark C-ZSM-5 and the state-of-the-art Nano-ZSM-5 give very low (10.65%) and medium (48.40%) conversion, respectively. In contrast, OMMS-ZSM-5(400,30), used as a representative sample, is the most active, with a conversion of 55.06%. Considering their similar Si/Al ratio (20-30) and acidities (Table S3), the improved catalytic activities in the conversion of bulky molecules over OMMS-ZSM-5(400,30) are directly related to the leaf-like open and interconnected intracrystalline ordered hierarchically micro-meso-macroporous architecture.

The performance boost is further evidenced in the MTO process. It is well known that the delayed transport of the reactants and products in zeolite channels usually accelerates the accumulation of coke, which in turn blocks the micropores and negatively affects not only the lifetime, the zeolite utilization efficiency, but also the selectivity of the zeolite catalyst.⁴⁶⁻⁴⁹ Thus, microporous zeolites are very sensitive to deactivation due to coke formation. For a better comparison, all the catalytic tests are made under harsh conditions with a high weight hourly space velocity (WHSV) of 3.6 h⁻¹ (See Experimental procedures). It is clearly seen (Figure 4A, Table 1) that C-ZSM-5 suffers from a rapid deactivation after only ~2.4 h on stream, much earlier than Nano-ZSM-5 (9.0 h). The life time extension of OMMS-ZSM-5(400,30) is 5 and 1.4 times longer than C-ZSM-5 and Nano-ZSM-5, respectively (Figure 4A and Table 1). The selectivity of ethylene and propylene (Figures 4A, S20-S21) is found to be ~45% over C-ZSM-5 and from 45% to 40% over Nano-ZSM-5 with time on stream. The highest selectivity (~50%) to ethylene and propylene is observed for OMMS-ZSM-5(400,30). More importantly, such high selectivity to light olefins remains almost constant during the whole catalytic testing. The average coking rate is only 3.92 mg g⁻¹ h⁻¹ for OMMS-ZSM-5(400,30), much lower than 8.88 mg g⁻¹ h⁻¹ and 7.15 mg g⁻¹ h⁻¹ for C-ZSM-5 and Nano-ZSM-5, respectively (Table 1). The above results show that not only our OMMS-ZSM-5(400,30) sample gives the highest selectivity to ethylene and propylene in MTO reaction, but also its average deactivation rate is 3.2 and 2.3 times lower than that of C-ZSM-5 and Nano-ZSM-5 catalysts, respectively.

More importantly, the catalytic performances of OMMS-ZSM-5 in MTO process

can be significantly improved by varying the Si/Al ratio and, in particular, intra-crystalline mesopore and macropore size. A clear correlation between the Si/Al ratio and the deactivation behaviour is evidenced in Figure 4B and Table 1. A higher Si/Al molar ratio in the zeolite catalyst results in a lower deactivation rate and a reduced coke formation rate of the catalysts, leading to a longer life time in the MTO reaction (Figure 4B and Table 1). The correlation between the Si/Al ratio and catalyst lifetime appears to be linear in the tested OMMS-ZSM-5s with the sphere size of 400 nm. By increasing Si/Al ratio from 30 to 100, the life time of OMMS-ZSM-5(400,100) (Si/Al = 100) (20.4 h) is nearly two folds longer than that of OMMS-ZSM-5(400,30) (Si/Al = 30). The Si/Al molar ratio of our ZSM-5 single crystals has only a minor effect on their final catalytic selectivity of ethylene and propylene, with all values staying between 45% and 50%. The interconnection and the size of their intra-crystalline micro-meso-macropores are therefore crucial factors in determining their catalytic lifetime (Figure 4B and Table 1). Among all the samples, OMMS-ZSM-5(600,100) with the largest mesopore and macropore sizes exhibits the lowest coke formation rate ($1.01 \text{ mg g}^{-1}\text{h}^{-1}$), being 8.9 and 7.2 times lower than that of C-ZSM-5 and Nano-ZSM-5 catalysts and the longest life time (31 h), being 13 and 3.5 times longer than that of C-ZSM-5 and Nano-ZSM-5 catalysts, respectively. As the benchmark C-ZSM-5 and the state-of-the-art Nano-ZSM-5 contain only micro-mesoporosity and micro-macroporosity, respectively, we attribute the above excellent catalytic performance to the improved diffusion behavior of the embedded larger intracrystalline pore size (Table S1) and to the completely open hierarchically interconnected and ordered micro-meso-macroporous structure of the ZSM-5 single crystals. As a result, the products can easily escape from the microporous channels and side reactions are significantly avoided, leading to a high propylene and ethylene selectivity, a much lower coke formation and deactivation rate and a substantial improvement in catalytic lifetime.^{50,51} A linear correlation between deactivation rate and average coke formation rate in MTO reaction is established among all tested ZSM-5 catalysts with different physico-chemical characteristics, irrespective of their microsize, nanosize, or interconnected hierarchical structure, or even different Si/Al molar ratio (Figure 4B). This further confirms that the resistance of zeolites to deactivation is mostly correlated with the suppression of coke formation. Consequently, accelerating the transport of reactants and products is of crucial importance in designing long-lived catalysts.

Diffusion Behavior and Catalytic Efficiency.

Generally, it is believed that both introducing an additional macro/mesopore system within an individual zeolite crystal and decreasing the crystal size can improve the accessibility of reactant molecules to the active sites of the zeolites. However, our findings demonstrate that an open, interconnected and intra-crystalline hierarchically ordered micro-meso-macroporous structure like in leaves is much more favorable. To illustrate the differences between our zeolite single crystals with interconnected micro-meso-macroporosity and the benchmark C-ZSM-5 with micro-mesoporosity and Nanosized ZSM-5 with micro-macroporosity in diffusion and catalytic efficiency, a kinetic study over 1,3,5-TIPB cracking reaction is performed. By Thiele modulus

analysis method (Equations 1-3 in Experimental procedures and Table S2), the utilization efficiency and effective diffusion length/rate in C-ZSM-5, Nano-ZSM-5 and OMMS-ZSM-5(400,30) are calculated. The variation of the effectiveness factor η related to the observed reaction rate as a function of the Thiele modulus ϕ^{48} is presented in Figure 4C and the η and ϕ values of studied zeolites are presented in Table S2. ϕ values drawn from C-ZSM-5, Nano-ZSM-5 and OMMS-ZSM-5(400,30) are significantly different (Table S2). Assuming that the diffusivity in all MFI microporous networks is the same,^{34,52} the obtained characteristic diffusion length L of Nano-ZSM-5 and OMMS-ZSM-5(400,30) are found to be shortened to 50% and 30%, respectively, compared to that of C-ZSM-5. The effective diffusion rate (D_{eff}/L^2 derived from $\frac{L_1}{L_2} = \frac{\varphi_1}{\varphi_2} \sqrt{\frac{k_2 D_{\text{eff},1}}{k_1 D_{\text{eff},2}}}$) of Nano-ZSM-5 is enhanced by two folds compared to C-ZSM-5 while that of OMMS-ZSM-5 (400,30) reaches 10 and 5 folds higher than that of C-ZSM-5 and Nano-ZSM-5, respectively, due to the effectively shortened diffusion length. The utilization efficiency η of C-ZSM-5 gives a generally observed value of 0.4 due to severe internal restricted diffusion because of large size of 1,3,5-TIPB molecule. That of Nano-ZSM-5 increases to 0.68 due to the large reduction in crystal size to nanometer scale, while OMMS-ZSM-5(400,30) reaches the highest and a high value η of 0.84. From Figure 4C, the OMMS-ZSM-5(400,30) is located in the full use regime while C-ZSM-5 in the diffusion limited regime, showing poor utilization efficiency of C-ZSM-5 catalyst in 1,3,5-TIPB cracking reaction and explaining its low catalytic activity and short life time. This is in excellent agreement with the MTO reaction results. By varying mesopore and macropore size within each of our ZSM-5 single crystals, the effective diffusion rate and catalyst utilization efficiency and performance can be further improved (Table 1 and Figure 4A). The continuous-flow variable-temperature hyperpolarized ^{129}Xe NMR (Figure S22) and the pulsed field gradient nuclear magnetic resonance (PFG NMR) techniques (Figure S23) comprehensively confirm the high quality, the excellent accessibility of the hierarchical pore network structures and interconnectivity in OMMS-ZSM-5.

To further compare the differences between the diffusion behavior and the accessibility to acid sites at dynamic condition of hierarchically porous zeolite single crystals, the benchmark C-ZSM-5 and the nanosized zeolite, an intelligent gravimetric analysis (IGA) on the diffusion of 1,3,5-trimethylbenzene (1,3,5-TMB) is performed under inert conditions (Figures 4D and S24, Tables 1 and S4 and Equation 4) in Experimental procedures). It is believed that only a few 1,3,5-TMB molecules (kinetic diameter = 0.78 nm) can penetrate the micropores (= 0.55 nm) while most of them will only be adsorbed on to the external surface of microporous zeolites. In comparison, the interparticular macropores of Nano-ZSM-5 and the ordered macro-mesoporous networks of OMMS-ZSM-5(400,30) offer sufficient space for more 1,3,5-TMB molecules. The relative diffusion rate of OMMS-ZSM-5(400,30) sample, which is calculated by linear fits of the normalized uptake profile (Q_t/Q_0), is 1.8 and 2.8 times higher than those in Nano-ZSM-5 and C-ZSM-5. The adsorption amount of 1,3,5-TMB at dynamic conditions at different diffusion time was measured for OMMS-ZSM-

5(400,30), OMMS-ZSM-5(600,100), C-ZSM-5 and Nano-ZSM-5 and is given in Figure S23 and Table S4. It is clearly seen that at dynamic condition, OMMS-ZSM-5 zeolite single crystals have much higher accessibility to acid sites than that of C-ZSM-5 and Nano-ZSM-5. This observation is directly linked to the excellent connectivity between micropores and meso-macropores of OMMS-ZSM-5 zeolite single crystals. The highest adsorption amounts of 1,3,5-TMB and the highest diffusivity observed for OMMS-ZSM-5 (600, 100) explain its best catalytic performance. All the results obtained by the laser hyperpolarized ^{129}Xe NMR, the PFG ^{129}Xe NMR, kinetic study of 1,3,5-TIPB cracking reaction, diffusion and dynamic accessibility of 1,3,5-TMB by IGA all in excellent consistence explains the excellent catalytic performance of OMMS-ZSM-5 zeolite single crystal. The highly ordered hierarchically micro-meso-macroporous structure of ZSM-5 single crystals is thus a decisive factor in improving the mass transfer property. By varying mesopore and macropore size within each of our ZSM-5 single crystals, the relative diffusion rate of OMMS-ZSM-5(600,100) with the largest mesopore and macropore size is found to be 7 and 4.5 times higher than that of C-ZSM-5 and Nano-ZSM-5. The above results show that the highly ordered and interconnected hierarchically macro-mesoporous structure inside our zeolite single crystal is much more effective than macroporous nanocrystals. Such unique hierarchically porous architecture can maximize the intracrystalline diffusion rate of reactants and products by reducing effective diffusion length, leading to a much higher zeolite utilization efficiency, a significant reduction in coking and deactivation rate and improved catalyst lifetime.^{53,54}

Conclusions

ZSM-5 single crystals with a highly interconnected and ordered intracrystalline macro-mesoporous system and variable Si/Al ratios and tunable mesopore and macropore size have been successfully synthesized by a bottom-up confined crystallization process. The hierarchical porous system in the single crystals results in a significantly improved diffusion performance for various reactants compared to the benchmark commercial micro-sized micro-mesoporous and micro-macroporous nanosized zeolite counterparts, leading to excellent catalytic performance in bulky molecules reaction and MTO process. Using OMMS-ZSM-5(400, 30) as example, not only the catalytic activity is much higher in bulky molecule cracking reaction, the effective diffusion rate of molecules reaches 10 and 5 folds higher than that of benchmark commercial micro-mesoporous C-ZSM-5 and the state-of-the-art micro-macroporous Nano-ZSM-5, respectively. Its utilization efficiency in 1,3,5-TIPB cracking reaction can reach a very high value of 0.84, which is doubled compared to that of C-ZSM-5 catalyst and 20% higher than that of Nano-ZSM-5 catalyst. The average coking rate in MTO reaction is 2.2 and 1.7 times lower than that for C-ZSM-5 and Nano-ZSM-5, respectively. Most importantly, the catalytic performances of our zeolite single crystals can be significantly improved by varying the Si/Al ratio and, in particular, by adjusting the intra-crystalline mesopore and macropore size. The relative diffusion rate of OMMS-ZSM-5(600, 100) with the largest mesopore and macropore size (Table 1) can reach even 7 and 4.5 times higher than that of C-ZSM-5 and Nano-ZSM-5, respectively, its average coking rate in

1 MTO reaction can attain 8.9 and 7.2 times lower than that for C-ZSM-5 and C-ZSM-5,
2 respectively. Compared to C-ZSM-5 and Nano-ZSM-5 catalysts, the life time of this
3 sample can be extended 13 and 3.5 times longer, respectively.

4 Our synthesis route to zeolite single crystals is not only simple and readily up-
5 scalable, but also highly versatile and has already been extended to the successful
6 synthesis of other zeolite structures and zeotype materials, including Beta, TS-1, MOR,
7 Y and SAPO-34. The utilization of such zeolite single crystals with excellent properties
8 to a large series of industrial catalytic reactions can lead to the design of innovative and
9 intensified reactors and processes with much highly enhanced efficiency, high catalytic
10 activity, selectivity and life time, minimum energy, time and raw material consumption.
11 The zeolite single crystal reactor concept can be exploited. Most importantly, our
12 synthesis strategy can be extended to fabricate single crystalline solids of any chemical
13 compositions such as transition metal oxides (TiO_2 , ZnO , ...), phosphate compounds,
14 silicate compounds,..., perovskites,... The key parameters to the construction of
15 hierarchical porous structure within each single crystal by our innovative confined
16 crystallization method are the control of the water content in the dried precursor gel and
17 the occupancy rate and the crystallization rate of dried precursor gel confined in the
18 hierarchical porous template. The utilization of such single crystalline solids in a
19 various reactions and procedures can lead to a revolution in industrial processes.

20

EXPERIMENTAL PROCEDURES

Resource Availability

Lead Contact

Further information and requests for resources and reagents should be directed to and will be fulfilled by the lead contact, Bao-Lian Su (bao-lian.su@unamur.be).

Materials Availability

OMMS-ZSM-5s generated in this study will be made available on request, but we may require a payment and/or a completed Materials Transfer Agreement if there is potential for commercial application.

Data and Code Availability

The data supporting the findings of this study are available in the article and Supplemental Information, or from the lead contact upon request.

Hierarchical zeolite single crystals preparation

Synthesis of uniform polystyrene (PS) spheres with tunable diameter

The uniform polystyrene (PS) spheres with a diameter of 220 nm were synthesized by emulsion polymerization. 0.6 g Sodium laurylsulfonate (emulsifying agent) was dissolved in 360 g deionized H₂O followed by addition of 47 g styrene. After adding 0.54 g potassium persulfate, the reaction was performed at 75 °C for 4.5 h under an argon atmosphere. Polystyrene spheres with monodispersed sizes of about 220 nm were obtained.

The uniform polystyrene (PS) spheres with a diameter of 420 nm were synthesized by soap-free polymerization. 47 g styrene were added in 400 g deionized H₂O followed by addition of 0.43 g potassium persulfate. The reaction was performed at 80 °C for 5 h under an argon atmosphere. Polystyrene spheres with monodispersed sizes of about 420 nm were obtained.

The uniform polystyrene (PS) spheres with a diameter of 620 nm were synthesized by soap-free polymerization. 49 g styrene were added in 430 g deionized H₂O followed by addition of 0.51 g potassium persulfate. The reaction was performed at 70 °C for 11 h under an argon atmosphere. Polystyrene spheres with monodispersed sizes of about 620 nm were obtained.

Synthesis of hierarchically ordered macro-mesoporous carbon (OMMC) with tunable diameter

In a typical procedure, the mass composition of the initial reaction mixtures is 100PS/15SiO₂/15C₁₂H₂₂O₁₁/1.5H₂SO₄, polystyrene spheres (as-synthesized) were first blended with silica sol (Ludox AS-40 colloidal silica) under magnetic stirring for 1 h. The obtained colloidal suspension was mixed with sucrose at room temperature for 10 min. Sulfuric acid was then slowly added under stirring for another 10 min to obtain a stable dispersion. The as-prepared dispersion was directly dried in an oven at 110 °C for 6 h, then at 160 °C for 6 h, followed by heating to 700 °C with a rate of 2 °C /min under pure nitrogen flow (1 L/min). The temperature was kept at 700 °C for 4 h to

decompose the polymer spheres and carbonize sucrose. The obtained carbon/silica composite was cooled in pure nitrogen and immersed in a 10 wt % hydrofluoric acid aqueous solution to remove silica, followed by washing with deionized water and drying at 60 °C to yield hierarchically ordered macro-mesoporous carbon (OMMC). The size of the macropores in OMMC can be tuned by varying the size of the corresponding polystyrene spheres (220 nm, 420 nm, 620 nm). OMMC templates with a macropore size of ~200 nm (OMMC-200), ~400 nm (OMMC-400) and ~600nm (OMMC-600) were obtained, respectively.

Synthesis of ordered and interconnected hierarchically macro-meso-microporous ZSM-5 single crystals (OMMS-ZSM-5s) with tunable meso-macroporosity and tunable Si/Al molar ratio:

Bottom-up confined crystallization process was used for the confined synthesis of hierarchical ordered macro-mesoporous ZSM-5 single crystals within the OMMC templates. In a typical synthesis, OMMC with different macropore size was impregnated with an excess solution of tetrapropylammonium hydroxide (TPAOH), tetraethyl orthosilicate (TEOS), aluminum isopropoxide and water. The molar composition of the initial reaction mixture is 0.36TPAOH /SiO₂/xAl₂O₃/19.2 H₂O (x=0.067, 0.040, 0.020). After slow evaporation of water from the mixture of the precursors confined in OMMC template at room temperature, the mixture was transferred to a Teflon-lined stainless-steel autoclave equipped with a porous metallic network suspended at the middle of the autoclave for holding the mixture. Sufficient water was placed at the bottom of autoclave to produce saturated steam. The steam-assisted crystallization (SAC) process was performed at 180 °C for 10 h. Thereafter, the samples were taken out of the autoclave and washed by filtration with abundant deionized water. Finally, the product was dried at 60°C and further calcined at 550 °C for 7 h to remove the carbon template. The as-synthesized samples are denoted by OMMS-ZSM-5(x,y) (OMMS represents ordered macro-mesoporous single-crystalline), where x and y represent the macropore size of OMMC templates and Si/Al molar ratio. In this work, OMMS-ZSM-5s with controllable mesopore and macropore size and tunable Si/Al ratio [OMMS-ZSM-5(200,100), OMMS-ZSM-5(400,100), OMMS-ZSM-5(600,100), OMMS-ZSM-5(400,30) and OMMS-ZSM-5(400,50)] were obtained.

Commercial micro-sized ZSM-5 (C-ZSM-5) and nano-sized ZSM-5 (Nano-ZSM-5) from FUYU New Materials Technology Co., Ltd. were used as reference samples with Si/Al ratios of 23 and 21, respectively.

Catalyst Characterization

XRD patterns were recorded on a Bruker D8 Advance diffractometer using CuK α monochromatized radiation (λ = 1.5418 Å). The measurements were taken at 45 kV and 40 mA in a continuous mode and a 2 θ range from 5° to 60° with a step increase of 0.02°.

Scanning electron microscope (SEM) images were obtained on a Hitachi S4800 field-emission SEM operated at 5 kV and 10 μ A. Transmission electron microscopy (TEM), high resolution transmission electron microscopy (HR-TEM), selected area electron diffraction (SAED) and high angle annular dark field scanning transmission

electron microscope (HAADF-STEM) studies were performed on a Thermo Fisher Titan Themis 60-300 'cubed' microscope fitted with double aberration-correctors for both TEM and STEM, operated at 120 kV. Three-dimensional (3D) reconstruction was performed through ASTRA Tomography Toolbox.

The chemical composition of the samples was determined by inductively coupled plasma (ICP) optical emission spectroscopy using a PerkinElmer Optima 4300DV. The wavelength range was 165~782 nm and resolution was 0.006 nm (at 200 nm).

Ar and N₂ adsorption-desorption isotherms were recorded using a Micromeritics ASAP 2020 gas sorptometer after the samples were degassed at 300 °C under vacuum for 12h. The micropore surface area was determined from Ar adsorption isotherm using t-plot method. By using the model based on non-local density functional theory (NLDFT), micropore volume and micropore size were derived from the adsorption branches of Ar isotherms with relative pressure p/p_0 of <0.01. The mesopore surface area was determined from N₂ adsorption using BET method. By using Barret-Joyner-Halenda (BJH) model, mesopore volume and mesopore size were determined by the adsorption branches of N₂ isotherms. Total pore volumes were estimated from the adsorbed amount at a relative pressure p/p_0 of 0.99.

Mercury intrusion porosimetry was performed with a Micromeritics Autopore IV 9500 operated in the pressure range from vacuum to 207 MPa. Samples were degassed in situ prior to measurement. The pore size distribution was determined by application of the Washburn equation. The macropore volume was determined by the volume of Hg intruded into pores of >50nm diameter.

The NMR spectra were recorded at room temperature, using a Varian VNMRS spectrometer operating at 9.4 T (²⁷Al freq. = 79.46 MHz; ²⁹Si freq = 79.46 MHz). The probe used was a Varian/Chemagnetics HX 4 mm CPMAS. The samples were packed in a standard 4 mm rotor and spun at 10 kHz. The number of transients range between ~200 and 11000 for the ²⁹Si spectra, and between 2000 and 3500 for the ²⁷Al spectra. For the ²⁷Al spectra, the parameters were: spectral width ~104 kHz, relaxation delay 100 ms, excitation pulse 3 μs, acquisition time 5 ms. For ²⁹Si spectra, the parameters were: spectral width ~104 kHz, relaxation delay 6 ms, excitation pulse 3 μs, acquisition time 5 ms.

Laser hyperpolarized ¹²⁹Xe NMR experiments were carried out at 110.6 MHz on a Varian Infinity-plus 400 spectrometer using a 7.5 mm probe. Before each experiment, samples (60–80 mesh) were dehydrated at 673 K under vacuum (<10⁻⁵ Torr) for 24 h. The optical polarization of xenon was achieved with a homemade apparatus with the optical pumping cell in the fringe field of the spectrometer magnet and a 60 W diode laser array (Coherent FAP-System). A flow of gas mixture (1% Xe – 1% N₂ – 98% He) was delivered at the rate of 100–150 mL min⁻¹ to the sample in the detection region via plastic tubing. Variable-temperature NMR measurements were performed in the range of 153–273 K. All one-dimensional spectra were acquired with 3.0 μs $\pi/2$ pulse, 100–200 scans, and 2 s recycle delay. The chemical shifts were referenced to the signal of xenon gas. Although the line of the xenon gas is temperature dependent, generally chemical shifts vary no more than 1 ppm in the temperature range of the experiments.

Prior to PFG NMR diffusion measurements, the sample was dehydrated on a

vacuum system at 673 K for 16 h. Then the samples were transferred into the NMR tube with pressure valve in glove box. After degassing overnight at 393 K, Xe was quantitatively introduced into NMR tube on a homemade uptake apparatus. After Xe adsorption, the tube was sealed and equilibrated at room temperature. The loading of adsorbed xenon was calculated by the ideal gas equation. All data were acquired at equilibrium condition. ^{129}Xe PFG NMR experiments were conducted on a 600 MHz Bruker Advance III spectrometer equipped with a 5 mm Diff50 diffusion probe delivering a maximum gradient of 1800 G cm^{-1} in the Z-direction. A bipolar-gradient stimulated echo sequence (STEBP, 13-interval pulse sequence) was applied in diffusion measurements in order to eliminate distortions of the PFG NMR results by internal magnetic field inhomogeneities (*i.e.* internal magnetic field gradients) induced by susceptibility variations in heterogeneous samples.

The acidity of the samples was determined by NH_3 temperature programmed desorption (TPD) using a Micromeritics ASAP 2920. For measurement, 50 mg sample powder was introduced into a quartz reactor and degassed under vacuum at 550°C . After cooling to room temperature, NH_3 gas was adsorbed for 1 h. This was followed by evacuation at 120°C to remove free and weakly adsorbed NH_3 . Desorption profile was then measured with evacuation at the temperature gradient of $10^\circ\text{C min}^{-1}$, using a thermal conductivity detector (TCD).

Catalytic Stability Test

For mechanical stability test, the samples were pressed under pressure at 5 MPa, 10 MPa and 15 MPa. The resultant samples were characterized by SEM and XRD.

For thermal stability test, the samples were treated in a muffle furnace at two different temperatures: 800°C and 1000°C for 1h. The resultant samples were characterized by SEM, XRD and Ar gas adsorption.

For hydrothermal stability test, the samples were pressed into moulds and placed into high temperature hydrothermal ageing tube under N_2 flow. Once the temperature reached to 780°C , N_2 flow was shut down. Then the samples were treated in saturated steam at 780°C for 2 h. The resultant samples were characterized by XRD and Ar gas adsorption.

Catalytic Activity Test

Before the catalytic activity evaluation, all the samples were converted into H^+ form. As a typical run, the sample was ion-exchanged with NH_4NO_3 (0.6 M) aqueous solution at 80°C for 3h, followed by calcination at 550°C for 6 h. This procedure was repeated three times. The methanol to olefines (MTO) reaction was performed in a stainless steel micro-catalytic-reactor. The catalyst sample (0.19 g) was first diluted with 1.81 g quartz sand into a well-distributed mixture and placed in micro-catalytic-reactor, was then preheated at 500°C for 1 h under N_2 flow (50 ml/min) beforehand. After settling the temperature at 480°C , methanol was uniformly pumped into a preheated device (180°C) to transform into vapor phase and then mixed with N_2 flow (90 ml/min) into a homogeneous phase. For a better and quick comparison, the tests under harsh conditions with a high weight hourly space velocity (WHSV) of methanol feedstock

was used. The WHSV was settled at 3.6 h⁻¹. The products were collected (time interval was 0.6 hour⁻¹ and analyzed by an on-line gas chromatograph (Agilent 6820) equipped with a flame ionization detector. For the conversion calculations, dimethyl ether (DME) was considered as a reactant rather than a product.

Kinetic Evaluation

Bulky 1,3,5-triisopropylbenzene (1,3,5-TIPB) cracking reaction was employed to quantitatively determine effective diffusivity and reactivity of different MFI zeolite catalysts. The reaction was taken in a specially-made stainless steel catalytic microreactor. 0.12g catalyst sample was dispersed in 4.68g quartz sand. Then the mixture was preheated at 500 °C for 1 h under N₂ flow before reaction. 1,3,5-TIPB was uniformly pumped into the preheated device to transform the liquid into vapor which was then mixed with N₂ as the carrier gas. The contact time was adjusted by changing the flow rate of the gas mixture. The catalytic activities of the zeolite samples were evaluated at different temperatures. The products were analyzed by an on-line gas chromatograph (Agilent 6820) equipped with a flame ionization detector. Before the catalytic test, the elimination of external diffusion was confirmed by establishing the conversion-contact time curves over different amounts of catalysts.

The rate constants of different zeolites in 1,3,5-TIPB cracking reaction at different temperatures and the reaction activation energy with/without diffusion limit (i.e. apparent/intrinsic activation energy, $E_{app,a}/E_{int,a}$) in zeolite catalysts have been calculated by fitting with Arrhenius equation. Thiele modulus φ is defined as Equation 1 and can be obtained by Equation 2. Effectiveness factor η was calculated by Equation 3 for zeolite with geometry of flat plate (thickness $2L$).

$$\varphi = \sqrt{\frac{r_{intrinsic}}{r_{diffusion}}} = L \sqrt{\frac{K}{D_{Aeff}}} \quad (\text{Equation 1})$$

where φ is the thiele modulus, $r_{intrinsic}$ is the max reaction rate, $r_{diffusion}$ is the max diffusion rate, L is the distance from the center of the catalyst pellet to the surface, K is the reaction rate constant, $D_{A,eff}$ is the effective diffusivity in the zeolite pores.

$$\frac{E_{app,a}}{E_{int,a}} = \frac{1}{2} + \varphi \frac{1 - \tanh h^2 \varphi}{2 \tanh h \varphi} \quad (\text{Equation 2})$$

where $E_{app,a}$ is the reaction activation energy with diffusion limit (i.e. apparent activation energy), $E_{int,a}$ is the reaction activation energy without diffusion limit (i.e. intrinsic activation energy), φ is the thiele modulus.

$$\eta = \frac{\tanh \varphi}{\varphi} \quad (\text{Equation 3})$$

where η is the effectiveness factor, φ is the thiele modulus.

Diffusion and Dynamic accessibility Test

1,3,5-trimethylbenzene diffusion measurement in ZSM-5 zeolites was performed using a computer-controlled intelligent gravimetric analyzer (IGA, Hiden Analytical Ltd., Warrington, UK). An ultrahigh vacuum system was employed by which adsorption isotherms and corresponding kinetics can be accurately acquired. A sensitive microbalance (resolution of 0.2 μg) was mounted in an enclosure with fitted thermostat

to remove thermal coefficients of the weighing system and thus provide high stability and accuracy. The zeolite sample (100 ± 1 mg) was degassed under vacuum ($<10^{-5}$ Pa) at $450\text{ }^{\circ}\text{C}$ for 10 h prior to the adsorption measurement. The system temperature was then set at $50\text{ }^{\circ}\text{C}$, regulated within $0.1\text{ }^{\circ}\text{C}$ by a water bath. The relative pressure was rapidly raised to 0.099 and then kept constant during the tests. For each step, the amount of adsorbate introduced in the system was kept small enough to keep the adsorption process isothermal. The weight increase of sorbents was automatically measured by a microbalance and continuously recorded as a function of time under the settled gas vapor pressure.

Diffusion coefficient D was obtained based on Fick's Law. Eqn (4) gives the fitting formula of diffusion coefficient D for zeolite with geometry of flat plate (thickness $h = 2L$) where Q_0 is the initial adsorbed quantity, Q_t is the intermediate adsorbed quantity, Q_{∞} is the equilibrium adsorbed quantity and D is diffusion coefficient.

$$\frac{Q_t - Q_0}{Q_{\infty} - Q_0} = 1 - \sum_{n=0}^{\infty} \frac{8}{[(2n+1)\pi]^2} \exp\left[\frac{-D(2n+1)^2\pi^2 t}{h^2}\right] \approx \frac{8}{\sqrt{\pi^2}} \left(\frac{D}{h^2}\right)^{1/2} \sqrt{t}$$

(when t is small) (Equation 4)

where Q_0 is the initial adsorbed quantity, Q_t is the intermediate adsorbed quantity, Q_{∞} is the equilibrium adsorbed quantity, n is the natural numbers, D is the diffusion coefficient for zeolite with geometry of flat plate (thickness $h = 2L$), t is the adsorbed time, h is the thickness of zeolite.

ACKNOWLEDGMENTS

This work is supported by Program for Changjiang Scholars and Innovative Research Team in University (IRT_15R52) of the Chinese Ministry of Education. B.-L. S. acknowledges the Chinese Ministry of Education for a "Changjiang Chaire Professor" position and a Clare Hall Life Membership, University of Cambridge. L.-H. C. acknowledges Hubei Provincial Department of Education for the "Chutian Scholar" program. Z.-Y. H. and G. V. T. acknowledge the support from the Center for Materials Research and Analysis and the State Key Laboratory of Silicate Materials for Architectures at Wuhan University of Technology. This work is also financially supported by NSFC-21671155, NSFC-U1663225, Major programs of technical innovation in Hubei (2018AAA012) and Hubei Provincial Natural Science Foundation (2018CFA054), Fundamental Research Funds for the Central Universities (WUT: 2018III039GX, 2019III012GX, 2020III002GX). We thank the 111 Project (Grant No. B20002) from the Ministry of Science and Technology and the Ministry of Education of China and the project "DepollutAir" of Interreg V France-Wallonie-Vlaanderen for supporting this work.

AUTHOR CONTRIBUTIONS

L.-H. C. and B.-L. S. conceived the project, L.-H. C., Z.-K. X., G. V. T., and B.-L. S. supervised the study, M.-H. S. designed and performed experiments, characterized samples, analyzed data and wrote the draft of the manuscript. J. Z. performed the catalysis reactions, analyzed the catalysis data and performed kinetic evaluation. Z.-Y.

H. and S. T., performed transmission electron microscopy and tomography analysis. L.-Y. L. and Y.-D. W. performed the diffusion test and analyzed the diffusion data. T. H. provided advice for the writing of this manuscript. L.-H. C. wrote the manuscript. L.-H. C., G. V. T., Z.-K. X., T. H. and B.-L. S. revised the manuscript and B.-L. S. finalized the manuscript.

DECLARATION OF INTERESTS

The authors declare no competing interests.

REFERENCES

1. Gallego, E. M., Portilla, M. T., Paris, C., León-Escamilla, A., Boronat, M., Moliner, M., and Corma, A. (2017). "Ab initio" synthesis of zeolites for preestablished catalytic reactions. *Science* 355, 1051-1054.
2. Jiao, F., Li, J., Pan, X., Xiao, J., Li, H., Ma, H., Wei, M., Pan, Y., Zhou, Z., Li, M. *et al.* (2016). Selective conversion of syngas to light olefins. *Science* 351, 1065-1068.
3. Slater, A. G., and Cooper, A. I. (2015). Function-led design of new porous materials. *Science* 348, aaa8075.
4. Snyder, B. E. R., Vanelderen, P., Bols, M. L., Hallaert, S. D., Böttger, L. H., Ungur, L., Pierloot, K., Schoonheydt, R. A., Sels, B. F., and Solomon, E. I. (2016). The active site of low-temperature methane hydroxylation in iron-containing zeolites. *Nature* 536, 317-321.
5. Schneider, D., Mehlhorn, D., Zeigermann, P., Kärger, J., and Valiullin, R. (2016). Transport properties of hierarchical micro-mesoporous materials. *Chem. Soc. Rev.* 45, 3439-3467.
6. Schwieger, W., Machoke, A. G., Weissenberger, T., Inayat, A., Selvam, T., Klumpp, M., and Inayat, A. (2016). Hierarchy concepts: classification and preparation strategies for zeolite containing materials with hierarchical porosity. *Chem. Soc. Rev.* 45, 3353-3376.
7. Lopez-Orozco, S., Inayat, A., Schwab, A., Selvam, T., and Schwieger, W. (2011). Zeolitic materials with hierarchical porous structures. *Adv. Mater.* 23, 2602-2615.
8. Hartmann, M., Machoke, A. G., and Schwieger, W. (2016). Catalytic test reactions for the evaluation of hierarchical zeolites. *Chem. Soc. Rev.* 45, 3313-3330.
9. Valtchev, V., Majano, G., Mintova, S., and Pérez-Ramírez, J. (2013). Tailored crystalline microporous materials by post-synthesis modification. *Chem. Soc. Rev.* 42, 263-290.
10. Sun, M.-H., Huang, S.-Z., Chen, L.-H., Li, Y., Yang, X.-Y., Yuan, Z.-Y., and Su, B.-L. (2016). Applications of hierarchically structured porous materials from energy storage and conversion, catalysis, photocatalysis, adsorption, separation, and sensing to biomedicine. *Chem. Soc. Rev.* 45, 3479-3563.
11. Zheng, X., Shen, G., Wang, C., Li, Y., Dunphy, D., Hasan, T., Brinker, C. J., and Su, B.-L. (2017). Bio-inspired murray materials for mass transfer and activity. *Nat. Commun.* 8, 14921.
12. Roth, W. J., Nachtigall, P., Morris, R. E., Wheatley, P. S., Seymour, V. R., Ashbrook, S. E., Chlubná, P., Grajciar, L., Položij, M., Zukal, A. *et al.* (2013). A family of zeolites with controlled pore size prepared using a top-down method. *Nat. Chem.* 5, 628-633.
13. Mitchell, S., Michels, N.-L., Kunze, K., and Pérez-Ramírez, J. (2012). Visualization of hierarchically structured zeolite bodies from macro to nano length scales. *Nat. Chem.* 4, 825-831.
14. De Jong, K. P., Zečević, J., Friedrich, H., De Jongh, P. E., Bulut, M., Van Donk, S., Kenmogne, R., Finiels, A., Hulea, V., and Fajula, F. (2010). Zeolite Y crystals with trimodal porosity as ideal

- hydrocracking catalysts. *Angew. Chem. Int. Ed.* 49, 10074-10078.
15. Qin, Z., Cychosz, K. A., Melinte, G., El Siblani, H., Gilson, J.-P., Thommes, M., Fernandez, C., Mintova, S., Ersen, O., and Valtchev, V. (2017). Opening the cages of faujasite-type zeolite. *J. Am. Chem. Soc.* 139, 17273-17276.
16. Jacobsen, C. J. H., Madsen, C., Houzvicka, J., Schmidt, I., and Carlsson, A. (2000). Mesoporous zeolite single crystals. *J. Am. Chem. Soc.* 122, 7116-7117.
17. Fan, W., Snyder, M. A., Kumar, S., Lee, P.-S., Yoo, W. C., McCormick, A. V., Penn, R. L., Stein, A., and Tsapatsis, M. (2008). Hierarchical nanofabrication of microporous crystals with ordered mesoporosity. *Nat. Mater.* 7, 984-991.
18. Lee, P.-S., Zhang, X., Stoeger, J. A., Malek, A., Fan, W., Kumar, S., Yoo, W. C., Al Hashimi, S., Penn, R. L., Stein, A. *et al.* (2011). Sub-40 nm zeolite suspensions via disassembly of three-dimensionally ordered mesoporous-imprinted silicalite-1. *J. Am. Chem. Soc.* 133, 493-502.
19. Liu, D., Bhan, A., Tsapatsis, M., and Al Hashimi, S. (2011). Catalytic behavior of Brønsted acid sites in MWW and MFI zeolites with dual meso- and microporosity. *ACS Catal.* 1, 7-17.
20. Chen, H., Wydra, J., Zhang, X., Lee, P.-S., Wang, Z., Fan, W., and Tsapatsis, M. (2011). Hydrothermal synthesis of zeolites with three-dimensionally ordered mesoporous-imprinted structure. *J. Am. Chem. Soc.* 133, 12390-12393.
21. Machoke, A. G., Beltran, A. M., Inayat, A., Winter, B., Weissenberger, T., Kruse, N., Güttel, R., Spiecker, E., and Schwieger, W. (2015). Micro/macroporous system: MFI-type zeolite crystals with embedded macropores. *Adv. Mater.* 27, 1066-1070.
22. Weissenberger, T., Reiprich, B., Machoke, A. G. F., Klühspies, K., Bauer, J., Dotzel, R., Casci, J. L., and Schwieger, W. (2019). Hierarchical MFI type zeolites with intracrystalline macropores: the effect of the macropore size on the deactivation behaviour in the MTO reaction. *Catal. Sci. Technol.* 9, 3259-3269.
23. Weissenberger, T., Machoke, A. G., Bauer, J., Dotzel, R., Casci, J., Hartmann, M., and Schwieger, W. (2020). Hierarchical ZSM-5 catalysts: the effect of different intracrystalline pore dimensions on catalyst deactivation behaviour in the MTO reaction. *ChemCatChem* 12, 2461-2468.
24. Weissenberger, T., Leonhardt, R., Zubiri, B. A., Pitínová-Štekrová, M., Sheppard, T. L., Reiprich, B., Bauer, J., Dotzel, R., Kahnt, M., Schropp, A. *et al.* (2019). Synthesis and characterisation of hierarchically structured titanium silicalite-1 zeolites with large intracrystalline macropores. *Chem. Eur. J.* 25, 14430-14440.
25. Na, K., Jo, C., Kim, J., Cho, K., Jung, J., Seo, Y., Messinger, R. J., Chmelka, B. F., and Ryoo, R. (2011). Directing zeolite structures into hierarchically nanoporous architectures. *Science* 333, 328-332.
26. Xu, D., Ma, Y., Jing, Z., Han, L., Singh, B., Feng, J., Shen, X., Cao, F., Oleynikov, P., Sun, H. *et al.* (2014). π - π interaction of aromatic groups in amphiphilic molecules directing for single-crystalline mesostructured zeolite nanosheets. *Nat. Commun.* 5, 4262.
27. Liu, F., Willhammar, T., Wang, L., Zhu, L., Sun, Q., Meng, X., Carrillo-Cabrera, W., Zou, X., and Xiao, F.-S. (2012). ZSM-5 zeolite single crystals with *b*-axis-aligned mesoporous channels as an efficient catalyst for conversion of bulky organic molecules. *J. Am. Chem. Soc.* 134, 4557-4560.
28. Zhu, J., Zhu, Y., Zhu, L., Rigutto, M., van der Made, A., Yang, C., Pan, S., Wang, L., Zhu, L., Jin, Y. *et al.* (2014). Highly mesoporous single-crystalline zeolite Beta synthesized using a nonsurfactant cationic polymer as a dual-function template. *J. Am. Chem. Soc.* 136, 2503-2510.
29. Pérez-Ramírez, J., Christensen, C. H., Egeblad, K., Christensen, C. H., and Groen, J. C. (2008).

- Hierarchical zeolites: enhanced utilisation of microporous crystals in catalysis by advances in materials design. *Chem. Soc. Rev.* 37, 2530-2542.
30. Cychosz, K. A., Guillet-Nicolas, R., García-Martínez, J., and Thommes, M. (2017). Recent advances in the textural characterization of hierarchically structured nanoporous materials. *Chem. Soc. Rev.* 46, 389-414.
 31. Mitchell, S., Pinar, A. B., Kenvin, J., Crivelli, P., Karger, J., and Pérez-Ramírez, J. (2015). Structural analysis of hierarchically organized zeolites. *Nat. Commun.* 6, 8633.
 32. Groen, J. C., Peffer, L. A. A., and Pérez-Ramírez, J. (2003). Pore size determination in modified micro- and mesoporous materials. Pitfalls and limitations in gas adsorption data analysis. *Micropor. Mesopor. Mat.* 60, 1-17.
 33. Michels, N.-L., Mitchell, S., Milina, M., Kunze, K., Krumeich, F., Marone, F., Erdmann, M., Marti, N., and Pérez-Ramírez, J. (2012). Hierarchically structured zeolite bodies: assembling micro-, meso-, and macroporosity levels in complex materials with enhanced properties. *Adv. Funct. Mater.* 22, 2509-2518.
 34. Gueudré, L., Milina, M., Mitchell, S., and Pérez-Ramírez, J. (2014). Superior mass transfer properties of technical zeolite bodies with hierarchical porosity. *Adv. Funct. Mater.* 24, 209-219.
 35. Thibault-Starzyk, F., Stan, I., Abelló, S., Bonilla, A., Thomas, K., Fernandez, C., Gilson, J.-P., and Pérez-Ramírez, J. (2009). Quantification of enhanced acid site accessibility in hierarchical zeolites – the accessibility index. *J. Catal.* 264, 11-14.
 36. Zubiaga, A., Warringham, R., Boltz, M., Cooke, D., Crivelli, P., Gidley, D., Pérez-Ramírez, J., and Mitchell, S. (2016). The assessment of pore connectivity in hierarchical zeolites using positron annihilation lifetime spectroscopy: instrumental and morphological aspects. *Phys. Chem. Chem. Phys.* 18, 9211-9219.
 37. Kenvin, J., Mitchell, S., Sterling, M., Warringham, R., Keller, T. C., Crivelli, P., Jagiello, J., and Pérez-Ramírez, J. (2016). Quantifying the complex pore architecture of hierarchical faujasite zeolites and the impact on diffusion. *Adv. Funct. Mater.* 26, 5621-5630.
 38. Liu, Y., Zhang, W., Liu, Z., Xu, S., Wang, Y., Xie, Z., Han, X., and Bao, X. (2008). Direct observation of the mesopores in ZSM-5 zeolites with hierarchical porous structures by laser-hyperpolarized ^{129}Xe NMR. *J. Phys. Chem. C* 112, 15375-15381.
 39. Chen, L.-H., Xu, S.-T., Li, X.-Y., Tian, G., Li, Y., Rooke, J. C., Zhu, G.-S., Qiu, S.-L., Wei, Y.-X., Yang, X.-Y. *et al.* (2012). Multimodal Zr-silicalite-1 zeolite nanocrystal aggregates with interconnected hierarchically micro-meso-macroporous architecture and enhanced mass transport property. *J. Colloid Interf. Sci.* 377, 368-374.
 40. Galarneau, A., Guenneau, F., Gedeon, A., Mereib, D., Rodriguez, J., Fajula, F., and Coasne, B. (2016). Probing interconnectivity in hierarchical microporous/mesoporous materials using adsorption and nuclear magnetic resonance diffusion. *J. Phys. Chem. C* 120, 1562-1569.
 41. Kärger, J., and Valiullin, R. (2013). Mass transfer in mesoporous materials: the benefit of microscopic diffusion measurement. *Chem. Soc. Rev.* 42, 4172-4197.
 42. Milina, M., Mitchell, S., Cooke, D., Crivelli, P., and Pérez-Ramírez, J. (2015). Impact of pore connectivity on the design of long-lived zeolite catalysts. *Angew. Chem. Int. Ed.* 54, 1591-1594.
 43. Zhang, S., Chen, L., Zhou, S., Zhao, D., and Wu, L. (2010). Facile synthesis of hierarchically ordered porous carbon via *in situ* self-assembly of colloidal polymer and silica spheres and its use as a catalyst support. *Chem. Mater.* 22, 3433-3440.
 44. Li, F., Wang, Z., and Stein, A. (2007). Shaping mesoporous silica nanoparticles by disassembly of

- hierarchically porous structures. *Angew. Chem. Int. Ed.* 46, 1885-1888.
45. Kokotailo, G. T., Lawton, S. L., Olson, D. H., and Meier, W. M. (1978). Structure of synthetic zeolite ZSM-5. *Nature* 272, 437-438.
46. Weckhuysen, B. M., and Yu, J. (2015). Recent advances in zeolite chemistry and catalysis. *Chem. Soc. Rev.* 44, 7022-7024.
47. Milina, M., Mitchell, S., Crivelli, P., Cooke, D., and Pérez-Ramírez, J. (2014). Mesopore quality determines the lifetime of hierarchically structured zeolite catalysts. *Nat. Commun.* 5, 3922.
48. Losch, P., Pinar, A. B., Willinger, M. G., Soukup, K., Chavan, S., Vincent, B., Pale, P., and Louis, B. (2017). H-ZSM-5 zeolite model crystals: structure-diffusion-activity relationship in methanol-to-olefins catalysis. *J. Catal.* 345, 11-23.
49. Olsbye, U., Svelle, S., Bjørgen, M., Beato, P., Janssens, T. V., Joensen, F., Bordiga, S., and Lillerud, K. P. (2012). Conversion of methanol to hydrocarbons: how zeolite cavity and pore size controls product selectivity. *Angew. Chem. Int. Ed.* 51, 5810-5831.
50. Bibby, D. M., Howe, R. F., and McLellan, G. D. (1992). Coke formation in high-silica zeolites. *Appl. Catal. A: Gen.* 93, 1-34.
51. Bibby, D. M., Milestone, N. B., Patterson, J. E., and Aldridge, L. P. (1986). Coke formation in zeolite ZSM-5. *J. Catal.* 97, 493-502.
52. Groen, J. C., Zhu, W. D., Brouwer, S., Huynink, S. J., Kapteijn, F., Moulijn, J. A., and Pérez-Ramírez, J. (2007). Direct demonstration of enhanced diffusion in mesoporous ZSM-5 zeolite obtained via controlled desilication. *J. Am. Chem. Soc.* 129, 355-360.
53. Zhao, L., Shen, B., Gao, J., and Xu, C. (2008). Investigation on the mechanism of diffusion in mesopore structured ZSM-5 and improved heavy oil conversion. *J. Catal.* 258, 228-234.
54. Baur, R., and Krishna, R. (2005). The effectiveness factor for zeolite catalysed reactions. *Catal. Today* 105, 173-179.

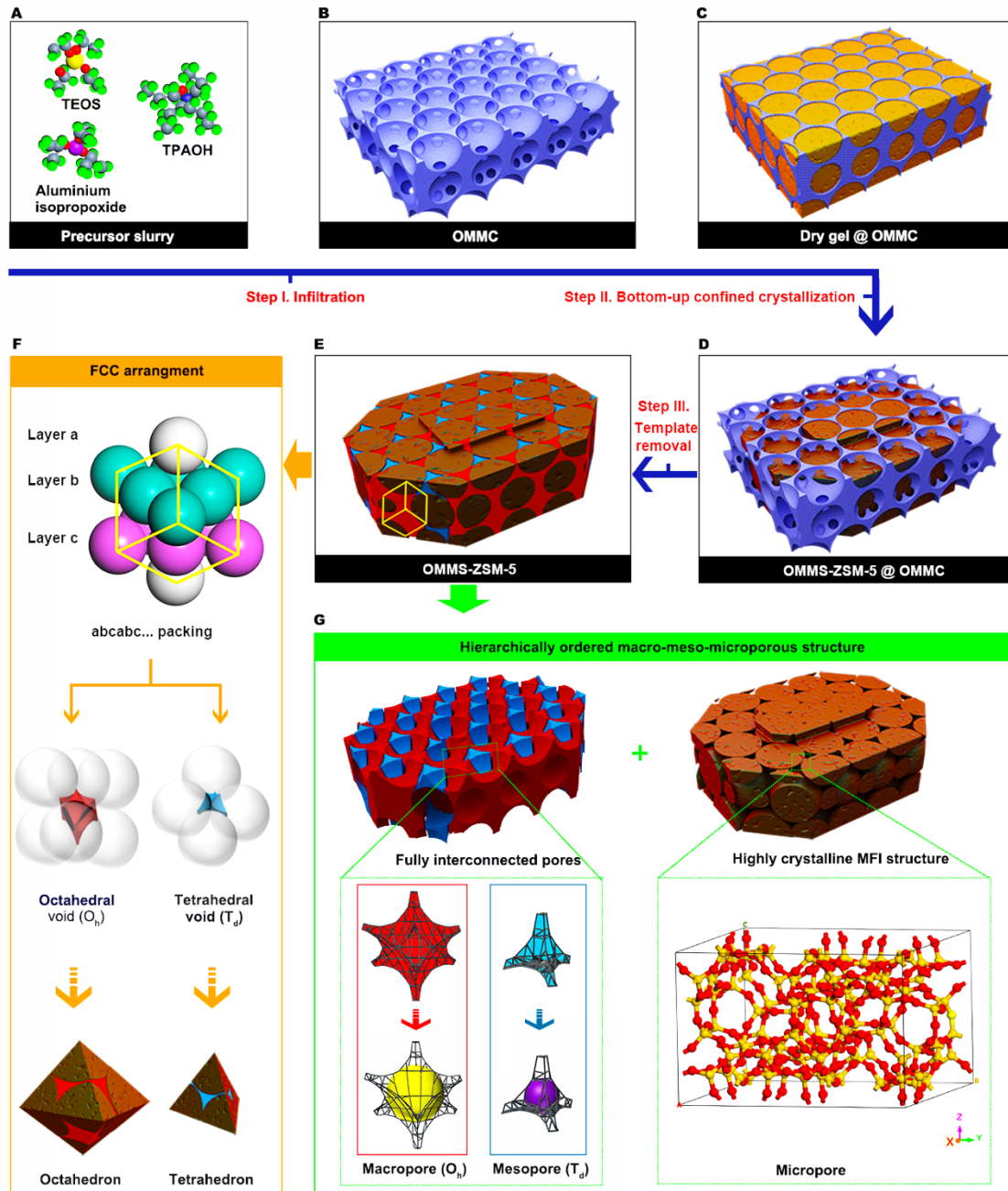


Figure 1. Synthesis and structure of OMMS-ZSM-5

(A-E) Schematic illustration of the synthesis route of OMMS-ZSM-5.

(F) The enlarged image of the selected yellow cubic area in (E), confirming the *abcabc...* stacking in FCC arrangement. The units in layer *a* are shaded white, those in layer *b* are green and those in layer *c* are pink. Such FCC arrangement contains two voids: the tetrahedral void (T_d , blue) and the octahedral void (O_h , red).

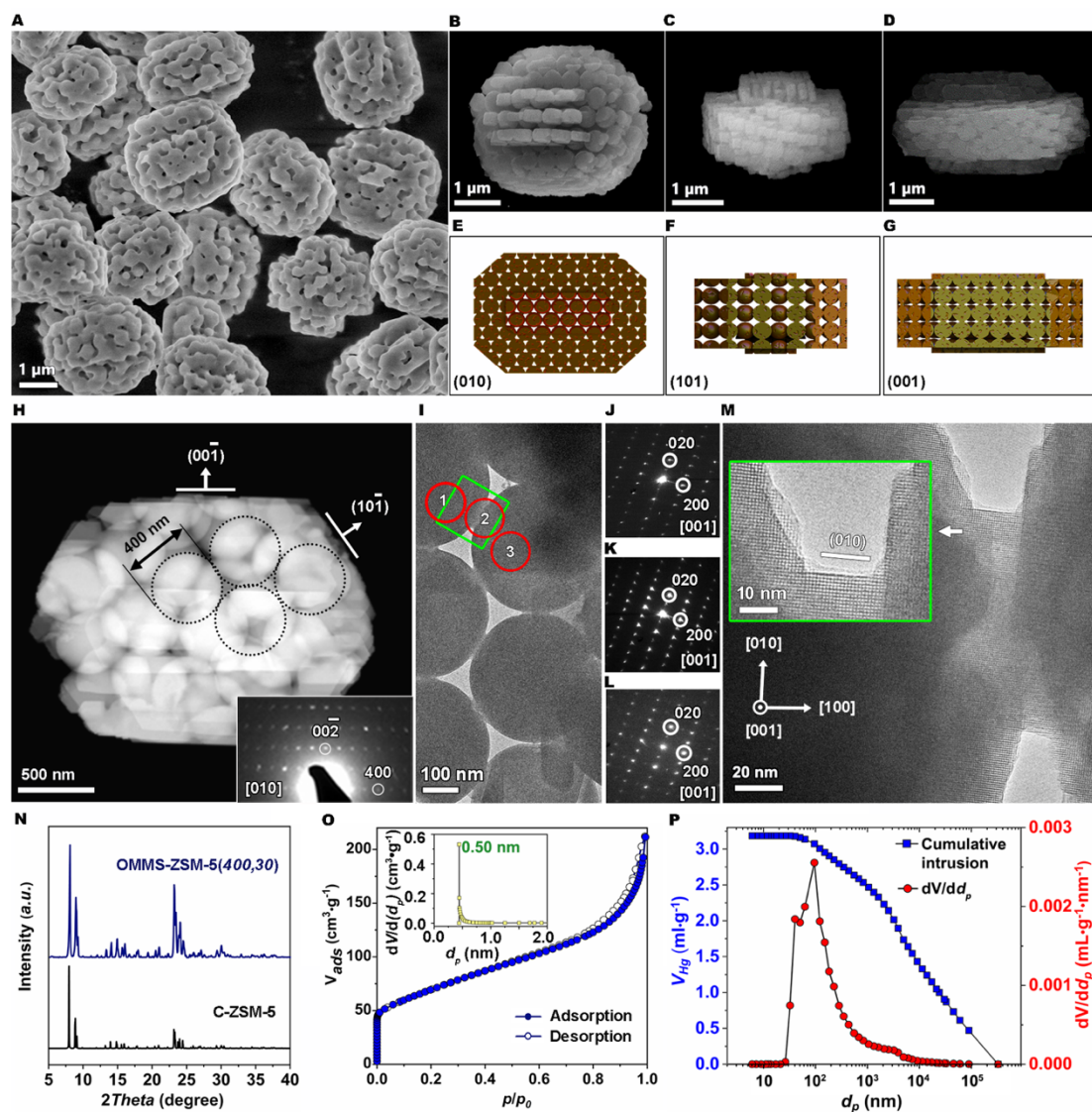


Figure 2. Characterization of OMMS-ZSM-5

(A-D) SEM images of OMMS-ZSM-5(400,30).

(E-G) Schematics of an individual crystal from three directions corresponding to B-D.

(H) HAADF-STEM image and ED pattern (inset) of an individual zeolite.

(I) TEM image of enlarged area in (H).

(J-L) SAED patterns of zones 1(J), 2 (K) and 3 (L) in (I).

(M) HRTEM images of green area in (I) with enlarged intergrowth region inset.

(N-P) XRD pattern (N), Argon adsorption-desorption isotherms (O) and micropore-size distribution (inset) and mercury intrusion (P) of OMMS-ZSM-5(400,30).

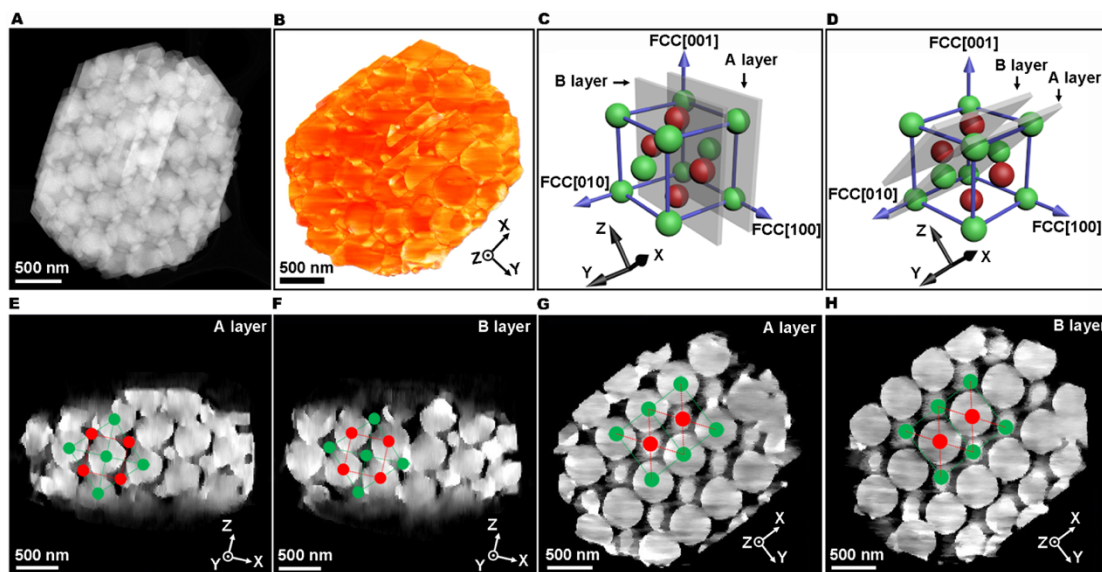


Figure 3. STEM tomography of OMMS-ZSM-5

(A and B) HAADF-STEM image (A) and corresponding 3D tomographic reconstruction (B) of an individual OMMS-ZSM-5(400,30) crystal.

(C and D) Schematic illustration of the FCC unit along the Y (C) and Z (D) axis.

(E and F) HAADF-STEM images of two adjacent orthoslices obtained from the 3D reconstruction: A layer (E) and B layer (F) (XZ plane, perpendicular to the Y axis).

(G and H) HAADF-STEM images of two adjacent orthoslices obtained from the 3D reconstruction: A layer (G) and B layer (H) (XY plane, perpendicular to the Z axis).

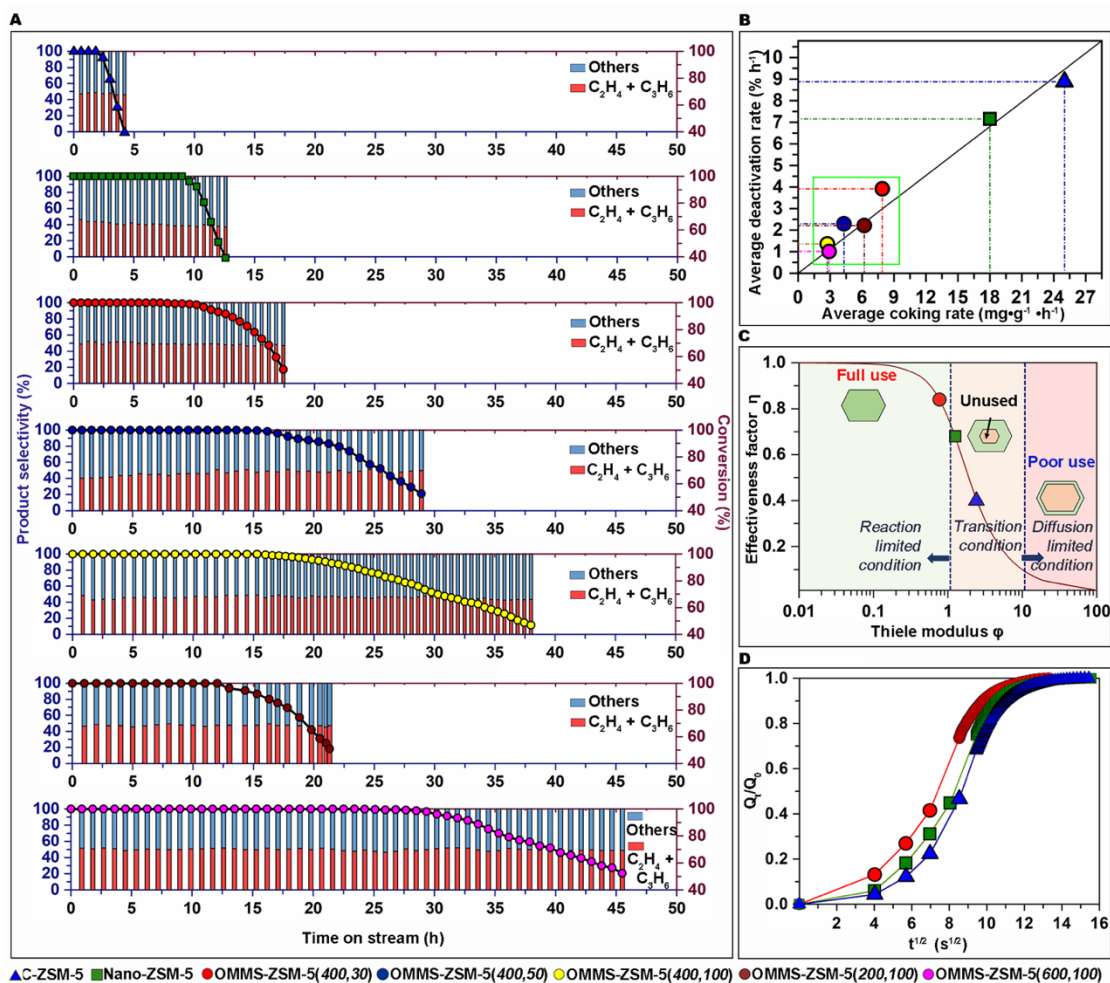


Figure 4. Catalytic performance, effectiveness factor and diffusion effectiveness of OMMS-ZSM-5

(A) Catalytic performances over various catalysts in the MTO reaction. Circles denote CH_3OH and DME conversion, whereas bars represent product selectivities.

(B) The correlation between the average coking rate and the deactivation rate of different catalysts.

(C) Effectiveness factor η as a function of Thiele modulus ϕ of different catalysts in the cracking of 1,3,5-triisopropylbenzene.

(D) Normalized uptake (Q_t/Q_0) profiles of 1,3,5-trimethylbenzene over different catalysts.

1 **Table 1. Catalytic activities for MTO reactions over various catalysts**

Catalyst	Si/Al ^{a)} [mol mol ⁻¹]	Life time ^{b)} [h ⁻¹]	Average deactivation rate ^{c)} [% h ⁻¹]	Coke amount [%]	Average Coke rate in MTO ^{d)} [mg g ⁻¹ h ⁻¹]	Relative diffusion rate ^{e)} [s ^{1/2}]
C-ZSM-5	23	2.4	25.0	3.73	8.88	0.0116
Nano-ZSM-5	21	9.0	18.0	9.01	7.15	0.0181
OMMS-ZSM-5 (400,30)	30	12.5	7.90	7.06	3.92	0.0330
OMMS-ZSM-5 (400,50)	50	18.5	4.31	6.62	2.29	0.0767
OMMS-ZSM-5 (400,100)	100	20.4	2.73	5.15	1.36	0.0477
OMMS-ZSM-5 (200,100)	100	14.1	6.20	4.72	2.21	0.0421
OMMS-ZSM-5 (600,100)	100	31.0	2.91	4.59	1.01	0.0805

2 ^{a)} determined by the elemental analysis (ICP).

3 ^{b)} the time for which the conversion of methanol exceeds 95%;

4 ^{c)} representing the percent loss of conversion from 95% to 50% per hour;

5 ^{d)} calculated by the mass loss per gram of catalyst over life time, the mass loss was accounted between
6 300°C and 700°C;

7 ^{e)} the slope of the fitted line in normalized uptake profile, in which $t^{1/2}$ of the drops lower than 2 s^{1/2}
8 (Equation 4 in Experimental procedures).

9

10

1 **Video S1. Zeolite spherical units that are densely stacked in a close-packed FCC**
2 **arrangement in an individual zeolite single crystal.**

3

4 **Video S2. 3D electron tomographic reconstruction of OMMS-ZSM-5(400,30).**

5

6